PCCP

PAPER

View Article Online
View Journal | View Issue

Cite this: *Phys. Chem. Chem. Phys.*, 2014, **16**, 17315

Reversible addition of the OH radical to *p*-cymene in the gas phase: multiple adduct formation. Part 2

Paulo Alarcón,[a] Birger Bohn,[b] Cornelius Zetzsch,*[ac] Marie-Thérèse Rayez*[d] and Jean-Claude Rayez*[d]

Received 13th May 2014,
Accepted 30th June 2014

DOI: 10.1039/c4cp02073a

www.rsc.org/pccp

A flash photolysis-resonance fluorescence (FP-RF) system was used to study the *p*-cymene (PC) + OH reaction at temperatures between 299 and 349 K in helium. Triexponential functions were fitted to groups of observed OH decay curves according to a model considering a reversible addition to form two adducts as thermolabile reservoirs of OH. Compared to Part 1 of this paper, consideration of a second adduct strongly improved the fits to our measurements, and the rate constants for the major pathways were optimized between 299 and 349 K. The Arrhenius expression for the rate constant of the sum of OH addition and H-atom abstraction pathways was found to be k_{OH} = 1.9 × 10^{-12} exp[(610 ± 210) K/*T*] cm^3 s^{-1}. Rate constants of unimolecular decomposition reactions of the adducts were similar to other aromatic compounds with the following Arrhenius expressions: 1 × 10^{12} exp[(−7600 ± 800) K/*T*] s^{-1} for adduct 1 and 4 × 10^{11} exp[(−8000 ± 300) K/*T*] s^{-1} for adduct 2. Adduct yields increased and decreased with temperature for adduct 1 and 2, respectively, but were similar (∼0.4) around room temperature. Equilibrium constants yielded values for reaction enthalpies and entropies of adduct formations. While for one adduct reasonable agreement was obtained with theoretical predictions, there were significant deviations for the other adduct. This indicates the presence of more than two adduct isomers that were not accounted for in the reaction model. Quantum chemical calculations (DFT M06-2X/6-31G(d,p)) and RRKM kinetics were employed with the aim of clarifying the mechanism of the OH addition to PC. These calculations show that formation of adducts with OH in *ortho* positions to the isopropyl and methyl substituents is predominant (55% and 24%) to those with OH in *ipso* positions (21% and 3%). A large fraction (>90%) of the *ipso*-C_3H_7 adduct is predicted to react by dealkylation forming *p*-cresol (in the absence of oxygen) and isopropyl radicals. These theoretical results agree well with the interpretation of the experimental results showing that the two *ortho* adducts (which appeared as OH reservoirs in the experiment) have been observed.

1. Introduction

Non methane volatile organic compounds (NMVOCs) are emitted into the atmosphere by anthropogenic and biogenic sources. It has been estimated that globally biogenic emissions significantly exceed anthropogenic emissions.[1,2] NMVOCs play a major role in the photochemical formation of ozone and secondary organic aerosols, and both processes are initiated by OH radicals, NO_3 radicals and O_3 oxidation.[3,4]

The biogenic aromatic compound *p*-cymene (1-methyl-4-isopropylbenzene or 4-isopropyltoluene) has four distinguishable positions where the OH radicals may add to the aromatic ring, as illustrated in Scheme 1: two equivalent ones *ortho* to the isopropyl group (PC_{ortho}–C_3H_7), two equivalent ones *ortho* to the methyl group (PC_{ortho}–CH_3), and two non-equivalent *ipso* positions at the site of the methyl and the isopropyl group (PC_{ipso}–CH_3 and PC_{ipso}–C_3H_7). Addition to an already occupied position (*ipso*-addition) is in general considered to be less important, but triexponential decays of OH have been observed by VUV flash photolysis/resonance fluorescence (FP-RF) in the presence of 1,3,5-trimethylbenzene, indicating that two different thermolabile adducts can regenerate OH.[5] The observation of hexamethyl-2,4-cyclohexadienone by GC-MS as the

[a] *Atmospheric Chemistry Research Laboratory, University of Bayreuth, 95448, Germany*
[b] *Institut für Energie - und Klimaforschung IEK-8: Troposphäre, Forschungszentrum Jülich, 52425 Jülich, Germany*
[c] *Fraunhofer Institute for Toxicology and Experimental Medicine, 30625 Hannover, Germany. E-mail: cornelius.zetzsch@uni-bayreuth.de*
[d] *Institut des Sciences Moleculaires, Université de Bordeaux, ISM UMR 5255, 33405 Talence, France. E-mail: mt.rayez@ism.u-bordeaux1.fr, jc.rayez@ism.u-bordeaux1.fr*

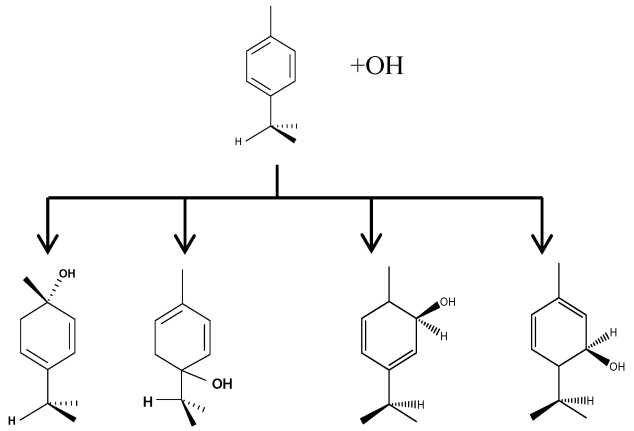

Scheme 1 *p*-Cymene + OH addition reactions, leading to the four adducts. From left to right: $PC_{ipso}-CH_3$, $PC_{ipso}-C_3H_7$, $PC_{ortho}-CH_3$ and $PC_{ortho}-C_3H_7$.

only product from the reaction of OH with hexamethylbenzene in the presence of NO_2 implies that an addition of OH is a major first step of this reaction.[6] Biexponential FP-RF-decays of OH in the presence of hexamethylbenzene as a prototype molecule, where *ipso* positions alone are available for addition, demonstrated a reversible reaction,[7] and the molecular ion of the adduct has been observed by single-photon VUV photoionization as an intermediate in a flow reactor very recently.[8] *Ipso*-type adducts may react by dealkylation and corresponding products from the reaction of toluene, *o*-, *m*-, and *p*-xylene with OH radicals have been observed by chemical ionization mass spectrometry in a flowtube study (5.4% phenol from toluene and similar yields of the cresols expected from dealkylation of the xylenes).[9] However, these results are not in agreement with an earlier smog chamber result of a phenol yield $<0.1\%$ from OH + toluene[10] and are not confirmed in a more recent smog chamber study with GC-FID analysis[11] that stated an upper limit of $<1\%$ formation of each cresol from OH + *m*-xylene and $<2\%$ for each cresol isomer from OH + *p*-cymene.

A total OH rate constant of $(15.1 \pm 4.1) \times 10^{-12}$ cm^3 s^{-1} was derived in a previous study on *p*-cymene[12] in a smog chamber at room temperature and 1 atm pressure of air. In another work,[11] the rate constant of H-atom abstraction was determined measuring the 4-methylacetophenone yield (the major product formed subsequent to the H-atom abstraction from the isopropyl substituent) and assuming a H-atom abstraction rate constant from the methyl substituent similar to the one determined for toluene. This led to an estimated $20 \pm 4\%$ contribution of abstraction to the overall OH rate constant. In our previous work,[13] the *p*-cymene + OH reaction was studied over a wide temperature range assuming a single adduct formation (biexponential model). This simplification was found to be satisfactory for temperatures below 320 K and higher than about 350 K, but between these temperatures our applied model could not describe the data. A preliminary study of the OH decay curves in the intermediate temperature range revealed that triexponential functions led to better fits to groups of observed curves than biexponential ones, indicating that more than one adduct was being formed. A similar behaviour has been observed for 1,3,5-trimethylbenzene, for which a kinetic model was proposed and the system of differential equations was solved.[5] In the present work we apply that new model of formation of two adducts (triexponential model) to the kinetic data previously[13] obtained on *p*-cymene by the flash photolysis-resonance fluorescence (FP-RF) technique over the temperature range between 297 and 350 K in helium buffer gas and perform theoretical calculations in order to identify the adducts, their energies and transition states.

2. Experimental

The experimental setup used in this work has been described elsewhere.[5,13–15] Briefly, OH radicals were generated by flash photolysis of water vapour using a Perkin Elmer FX 1165 short arc xenon flash lamp as photolytic light source at an energy of 540 mJ per flash. A quartz resonance lamp was mounted at right angles to the VUV photolysis beam and to the photomultiplier. A gas mixture of H_2O–He was allowed to flow through the resonance lamp. The electrodeless microwave discharge dissociated H_2O to produce electronically excited OH ($A^2\Pi$). The radiation leaving the lamp was focused into the observation zone exciting the photolytically produced OH radicals in the reaction cell.

The fluorescence from the reaction cell passed through a 308 nm interference filter and was focused onto the photocathode of a photomultiplier tube (Thorn-EMI, 9789QB). The signal was processed and accumulated using the photon-counting technique with a discriminator and a multichannel scaler board (EG&G Ortec, model ACE MCS) at a dwell time of 0.98 ms, corresponding to a total of 4 s observation time after the flash. The concentration of water vapour in the reaction cell was kept constant at 1.5×10^{15} cm^{-3}, leading to an estimated initial OH radical concentration of 2×10^{10} cm^{-3}.[16,17] The *p*-cymene concentration was varied between 5×10^{12} cm^{-3} and 43×10^{12} cm^{-3}, which is high enough to assure pseudo first order conditions for OH. In contrast

Table 1 Experimental conditions. Total pressure 203 ± 2 mbar of helium

Set #	T and ΔT/K		N^a	[*p*-Cymene] (min., max.)/10^{12} cm^{-3}	
1	299.0	0.2	28	5.1	38.8
2	314.6	0.5	43	4.9	39.2
3	316.8	0.5	15	7.0	42.1
4	324.1	0.3	22	7.6	43.4
5	325.9	0.2	36	7.0	42.2
6	326.0	1.8	9	6.7	16.4
7	327.3	0.0	12	7.5	19.8
8	328.5	0.0	57	7.1	42.9
9	329.9	0.2	22	7.3	42.4
10	332.0	0.2	58	6.9	42.6
11	334.2	0.3	21	4.8	39.6
12	334.3	0.2	20	7.2	32.3
13	335.3	0.2	20	6.7	42.1
14	335.7	0.2	26	6.6	39.8
15	336.2	0.0	66	7.1	42.7
16	339.9	1.0	38	5.8	41.6
17	343.5	0.2	18	6.9	41.7
18	345.2	0.1	23	7.3	42.3
19	348.0	0.4	19	7.4	41.7
20	348.9	0.1	45	4.8	39.3

[a] Number of measurements.

to our previous work,[13] only experiments performed with the xenon flash lamp were used as the set made with the N_2 spark discharge lamp seemed to be affected by impurities increasing the reactivity towards OH. The experimental conditions are summarized in Table 1. Differences between this table and Table 1 of the preceding part arise because some curves were removed from the biexponential fits. These curves were assumed to be deficient when the intensity ratio and lifetime of the first decay did not increase with increasing *p*-cymene concentration. The results presented in this work were obtained from all measurements as fits to individual decays were found to be difficult to perform at some combinations of temperature and *p*-cymene concentrations.

The gases used in this work had the following stated minimum purities: He (Rießner) – 99.996%; N_2 (Linde) – 99.999%. Liquid *p*-cymene (Aldrich) had a stated minimum purity of 99%. Deionized water was doubly distilled by a quartz still.

3. Theoretical approach

The reaction of OH with *p*-cymene (PC) is complex due to the presence of two alkyl chains, isopropyl and methyl, which differentiates each site of the molecule with respect to OH attack. The aim of the theoretical calculations is to shed some light into this complex mechanism and help to interpret the experimental results by presenting a comprehensive theoretical investigation of the OH attack on *p*-cymene. No theoretical investigation of this type has been reported so far on this system.

3.1 Computational details

All calculations were performed using the GAUSSIAN 09 package.[18] The geometries and energies were optimized using density functional theory (DFT) with the hybrid meta exchange–correlation functional M06-2X,[19] coupled to the split valence basis set 6-31G(d,p). This highly nonlocal M06-2X functional developed by Zhao and Truhlar[19] is well suited for structures and energetics, specifically for the determination of energy barriers. The unrestricted Hartree–Fock (UHF) formulation has been used since it is a convenient way to describe open-shell and bond-breaking processes. Its use is justified in our study because we did not observe any significant spin contamination for all the stationary points explored, the quantum average value $\langle S^2 \rangle$ of the square of the total spin operator remaining close to 0.75, *i.e.*, the characteristic value for a doublet state. Full geometry optimization has been performed throughout. We have checked carefully that all the saddle points found are correctly connected to two minima and are characterized by the existence of only one negative eigenvalue of the Hessian matrix corresponding to an imaginary frequency in the normal-mode analysis.

Since one of our goals is the determination of branching ratios of all the reactive channels, Transition State Theory (TST) is a convenient tool to determine rate constants. In terms of activation free energy $\Delta G^{\#}$, TST formula reads:

$$k_T \propto g\left(\frac{k_B T}{h}\right) \exp\left[\frac{-\Delta G_T^{\#}}{RT}\right] \quad (1)$$

where k_B and h are respectively the Boltzmann and Planck constants and g is the number of equivalent carbon atom sites. Our aim in these calculations is not to obtain absolute values for the rate constants, but rather to look at the relative reactivity of each carbon atom site with respect to OH.

4. Experimental results and discussion

4.1 Kinetic analysis and data evaluation

As outlined above the reversible addition of OH radicals to the aromatic ring in *p*-cymene can occur at four different positions, leading to the formation of adducts with potentially different properties. The decay curves of OH can deliver first hints about the quantity of distinguishable adducts formed. The initial fast decay corresponds to the consumption of OH radicals by H-atom abstraction and OH addition, while the subsequent slower OH decays are caused by regeneration of OH by a unimolecular decomposition of unstable adducts. A biexponential OH decay indicates the formation of only one adduct or the formation of several adducts with similar kinetic properties, whereas a triexponential OH decay indicates the formation of at least two distinguishable adducts.

Decays curves of OH in the presence of *p*-cymene were found to be mostly biexponential at temperatures below around 320 K and at temperatures above about 350 K (Fig. 1).[13] In the intermediate range deviations from biexponential behaviour were observed, and the following mechanism for the formation of two adduct species that results in triexponential decay curves was applied to fit the decay curves:[5]

$$\text{OH} + p\text{-cymene} \leftrightarrow \text{adduct}_1; \quad k_{11a}, k_{-11a} \quad \text{(R1)}$$

$$\text{OH} + p\text{-cymene} \leftrightarrow \text{adduct}_2; \quad k_{12a}, k_{-12a} \quad \text{(R2)}$$

$$\text{OH} + p\text{-cymene} \rightarrow \text{products}; \quad k_{1b} \quad \text{(R3)}$$

$$\text{OH} \rightarrow \text{loss}; \quad k_2 \quad \text{(R4)}$$

$$\text{adduct}_1 \rightarrow \text{loss}; \quad k_{31} \quad \text{(R5)}$$

$$\text{adduct}_2 \rightarrow \text{loss}; \quad k_{32} \quad \text{(R6)}$$

The rate equations that describe the change in the concentrations of OH radicals and of the adducts are shown below.

$$\frac{d}{dt}[\text{OH}] = -a[\text{OH}] + b[\text{adduct}_1] + e[\text{adduct}_2] \quad (2)$$

$$\frac{d}{dt}[\text{adduct}_1] = c[\text{OH}] - d[\text{adduct}_1] \quad (3)$$

$$\frac{d}{dt}[\text{adduct}_2] = f[\text{OH}] - g[\text{adduct}_2] \quad (4)$$

The combined first-order rate constants are given by:

$$a = k_2 + (k_{11a} + k_{12a} + k_{1b})[p\text{-cymene}] \quad (5)$$

$$b = k_{-11a} \quad (6)$$

$$c = k_{11a}[p\text{-cymene}] \quad (7)$$

$$d = k_{-11a} + k_{31} \quad (8)$$

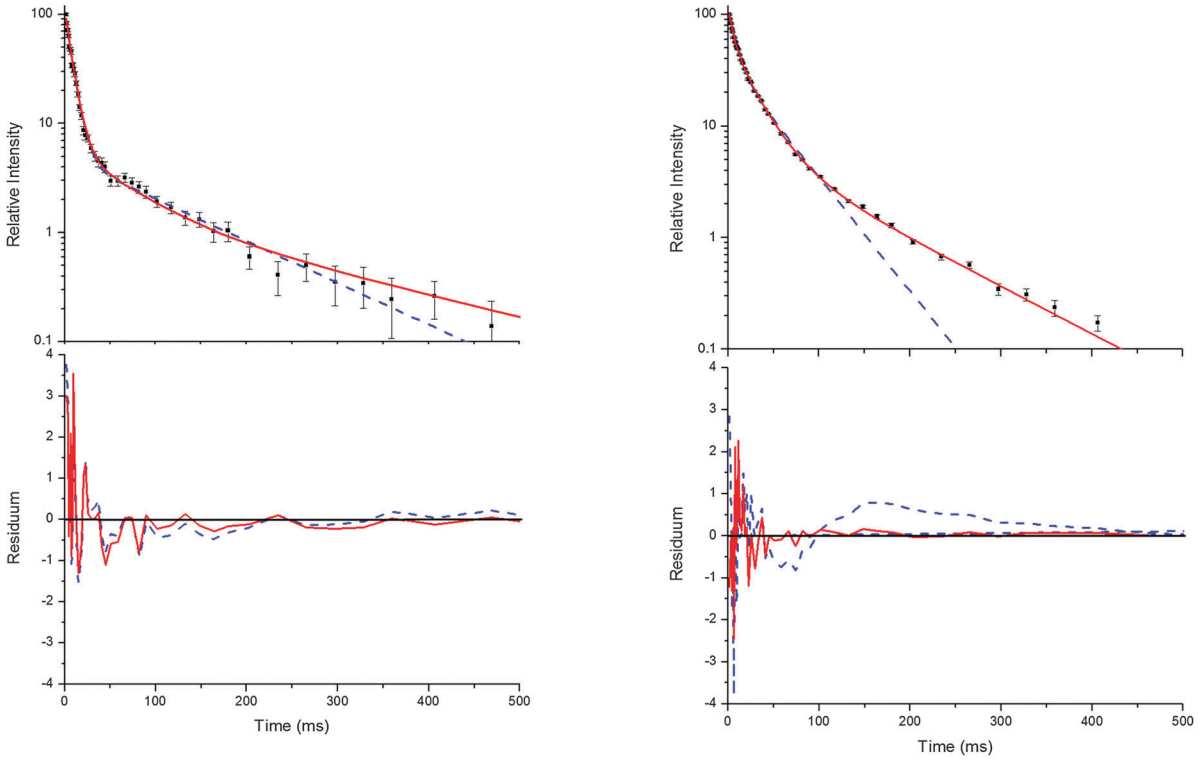

Fig. 1 Typical decay curves of OH (background subtracted), biexponential (blue dashed line) and triexponential (red solid line) model curves and fit residuals for measurements at 299 K (left side) and 330 K (right side) at a *p*-cymene concentration of 9×10^{12} cm^{-3} from simultaneous fits to a number (28 and 20 for the left and right side, respectively) of such curves at various concentrations. Obviously, the biexponential model curve satisfactorily describes the data at 299 K but not at 330 K while the triexponential model curves are applicable at both temperatures in agreement with the reaction model considering two adduct species ((R1)–(R6)).

$$e = k_{-12a} \quad (9)$$

$$f = k_{12a}[p\text{-cymene}] \quad (10)$$

$$g = k_{-12a} + k_{32} \quad (11)$$

Bohn and Zetzsch[5] proposed the mechanism shown above ((R1)–(R6)) for the reaction of the trimethylbenzenes with OH radicals and obtained the analytical solution of the corresponding system of differential equations. This solution allows us to determine the parameters *a*, *bc*, *d*, *ef*, and *g* for a set of measurements at a given temperature and total pressure. Details on the analytical solution and its limitations in terms of separable parameters are given elsewhere.[5] Although up to four different adducts can be formed in the OH reaction studied here, we confined our reaction model to two adduct species for two reasons. Firstly, because analytical solutions are not available for a greater number of adducts. Secondly, because the precision of the OH decay curves is too poor to permit a proper distinction of three or even four exponentials (Fig. 1).

Independent of the model applied, the approach has further limitations. If the decay time of the first exponential decay approaches the time resolution of our experiment (0.98 ms) fit results become distorted. Another limit is reached when the intensity ratio of the first and the second or third decay becomes too small. Then a small and quickly vanishing contribution of the first exponential remains, turning the decays into apparently bi- or monoexponentials. In this work, these limits were reached at temperatures larger than about 350 K and therefore higher temperatures were not considered.

Technical details on the fitting procedure and on the estimation of parameter uncertainties can be found elsewhere.[5,13] Error estimates for the exponential term in the Arrhenius and van't Hoff expressions were obtained by fitting the maximum and minimum parameter values, respectively. Due to the small temperature range, errors in the pre-exponential factors were large and therefore will not be presented here. Table 2 summarizes the combined rate constants for each isothermal set of measurements.

4.2 Background losses of OH radicals (k_2)

OH radicals may also react with minor impurities that can enter the cell from the dosing system (previous or present sample), the carrier gas or from wall desorption and leaks. Diffusion of OH radicals from the observation zone due to concentration gradient between the irradiated volume and the cell walls as well as transport due to the constant gas flow may contribute to the OH radical losses described by the rate constant k_2. This rate constant comprised several processes, and therefore its complete understanding is complicated and related to the experimental conditions applied. In this work, the average loss rate constant was found to be 4 s^{-1} in good agreement with the experimental lifetime of OH radicals in our system without any

Table 2 Rate constants fitted for the *p*-cymene + OH reaction system (reactions (R1)–(R6))

Set #	k_2/s^{-1}	$(k_{11a} + k_{12a} + k_{1b})/10^{-12}$ cm^3 s^{-1}	$(k_{11a}\,k_{-11a})/10^{-12}$ cm^3 s^{-2}	$k_{-11a} + k_{31}/s^{-1}$	$(k_{12a}\,k_{-12a})/10^{-12}$ cm^3 s^{-2}	$k_{-12a} + k_{32}/s^{-1}$
1	-9.9 ± 4.5	14.9 ± 0.9	$81 \pm {}^{18}_{21}$	$24 \pm {}^{18}_{2}$	$13 \pm {}^{25}_{10}$	6 ± 0.2
2	2.3 ± 2.1	13.1 ± 0.8	$303 \pm {}^{45}_{40}$	$52 \pm {}^{8}_{6}$	$11 \pm {}^{6}_{4}$	$7.1 \pm {}^{2.3}_{1.4}$
3	12.9 ± 1.9	12.7 ± 0.5	$310 \pm {}^{26}_{24}$	61 ± 5	$18 \pm {}^{5}_{4}$	10.3 ± 1.5
4	5.7 ± 2.1	12 ± 0.7	$443 \pm {}^{56}_{51}$	85 ± 7	15 ± 3	$10.4 \pm {}^{1.3}_{1.2}$
5	8.3 ± 1.8	11.9 ± 0.5	$496 \pm {}^{52}_{48}$	$92 \pm {}^{7}_{5}$	15 ± 3	$11 \pm {}^{1.4}_{1.1}$
6	5.4 ± 4.4	$14.7 \pm {}^{2.9}_{2.4}$	$919 \pm {}^{56}_{36}$	$107 \pm {}^{26}_{20}$	$17 \pm {}^{10}_{6}$	$10.2 \pm {}^{3.2}_{2.5}$
7	$6.5 \pm {}^{2.1}_{2}$	11.5 ± 0.7	$513 \pm {}^{88}_{77}$	99 ± 10	15 ± 3	$11.4 \pm {}^{1.4}_{1.3}$
8	7 ± 1.4	11.8 ± 0.5	$598 \pm {}^{62}_{57}$	109 ± 7	$17 \pm {}^{3}_{2}$	$12.2 \pm {}^{1}_{0.9}$
9	6.2 ± 0.1	11.7 ± 0.7	$684 \pm {}^{102}_{78}$	123 ± 10	18 ± 3	$13.1 \pm {}^{1.4}_{1.3}$
10	6.3 ± 1.2	11.7 ± 0.7	$791 \pm {}^{100}_{104}$	$141 \pm {}^{12}_{11}$	18 ± 2	13.9 ± 1.1
11	$0.1 \pm {}^{1.6}_{0.1}$	$12.4 \pm {}^{2.1}_{1.6}$	1255 ± 25	$189 \pm {}^{32}_{28}$	$19 \pm {}^{7}_{5}$	$16.1 \pm {}^{3.1}_{2.4}$
12	12.1 ± 1.8	10 ± 1	$713 \pm {}^{74}_{154}$	$152 \pm {}^{23}_{20}$	$26 \pm {}^{7}_{6}$	$20.3 \pm {}^{2.6}_{2.7}$
13	2.1 ± 1.3	$13 \pm {}^{1.3}_{1.2}$	1387 ± 28	$209 \pm {}^{22}_{20}$	28 ± 4	$18.8 \pm {}^{1.6}_{1.5}$
14	$6.8 \pm {}^{2.4}_{2.6}$	$13.1 \pm {}^{0.5}_{2.2}$	1541 ± 31	$203 \pm {}^{45}_{34}$	$29 \pm {}^{11}_{8}$	$19.2 \pm {}^{3.7}_{2.9}$
15	4.1 ± 1.1	11.7 ± 0.7	$1089 \pm {}^{22}_{144}$	$186 \pm {}^{15}_{14}$	$21 \pm {}^{3}_{2}$	$16.8 \pm {}^{1.4}_{1.3}$
16	4.9 ± 1.7	$11.1 \pm {}^{1.6}_{1.5}$	1450 ± 29	$241 \pm {}^{36}_{32}$	$27 \pm {}^{8}_{6}$	$22.5 \pm {}^{3.4}_{3.0}$
17	$0.8 \pm {}^{2.1}_{0.8}$	$11.3 \pm {}^{2.5}_{2.1}$	1854 ± 37	$309 \pm {}^{75}_{62}$	$35 \pm {}^{14}_{11}$	$29.8 \pm {}^{5.8}_{5.5}$
18	$0.1 \pm {}^{2.5}_{0.1}$	$12.6 \pm {}^{3.4}_{2.5}$	2520 ± 50	$354 \pm {}^{86}_{76}$	$35 \pm {}^{14}_{10}$	$30.6 \pm {}^{6.0}_{5.1}$
19	$-1.3 \pm {}^{4.8}_{1.3}$	$16.2 \pm {}^{6.9}_{4.9}$	$4860 \pm {}^{2500}_{970}$	$486 \pm {}^{155}_{127}$	$46 \pm {}^{27}_{18}$	$36.7 \pm {}^{8.9}_{7.9}$
20	$-1.6 \pm {}^{3.9}_{1.6}$	$10.6 \pm {}^{10.2}_{4.4}$	1847 ± 40	$360 \pm {}^{480}_{230}$	$35 \pm {}^{59}_{8}$	34.3 ± 19.4

reactant of about 3 s^{-1}. In contrast to the previous paper, applying the triexponential model to our measurements, some k_2 values were negative. This irregularity was found to have no effect on the determination of other combined rate constants, corroborated by the good agreement with other constants determined at similar temperatures.

4.3 OH + *p*-cymene ($k_{OH} = k_{11a} + k_{12a} + k_{1b}$)

Analogous to the biexponential model, the fitting procedure allows us to determine the total rate constant for the reaction between OH radicals and *p*-cymene, but not each rate constant individually. In the case of the triexponential model, the total rate constant consists of three rate constants: OH addition for the formation of adducts 1 (k_{11a}) and 2 (k_{12a}), and H-atom abstraction (k_{1b}). The total rate constant was found to be $(14.9 \pm 0.9) \times 10^{-12}$ cm^3 s^{-1} at 299 K. This value is in good agreement with the value published by Corchnoy and Atkinson $(15.1 \pm 4.1) \times 10^{-12}$ cm^3 s^{-1}.[12] At temperatures up to around 320 K, biexponential[13] and triexponential models show good agreement, but deviating results at higher temperatures where the fit quality for the biexponential model was also poor (Fig. 2). This behaviour was also observed for 1,3,5-trimethylbenzene,[5] an aromatic compound which can react with OH radicals to form two different adducts alone.

The Arrhenius expression for the total rate constant was determined as $k_{OH} = 1.9 \times 10^{-12} \exp(610 \pm 210)\ K/T$ cm^3 s^{-1}, comparable with the previously obtained for temperatures below 320 K.[13]

4.4 Forward and backward reactions ($k_{11a}k_{-11a}$; $k_{12a}k_{-12a}$)

The analytical solution of the differential equation system for the triexponential model does not allow us to separate the rate constants for the forward (k_{11a} and k_{12a}) and backward reactions (k_{-11a} and k_{-12a}), but allows us to determine their products ($k_{11a}k_{-11a}$ and $k_{12a}k_{-12a}$).[5] A semi-logarithmic plot of these products *versus* the inverse temperature (Fig. 3) was used to determine the sum of the activation energies for OH addition and unimolecular decay for each of the adducts.

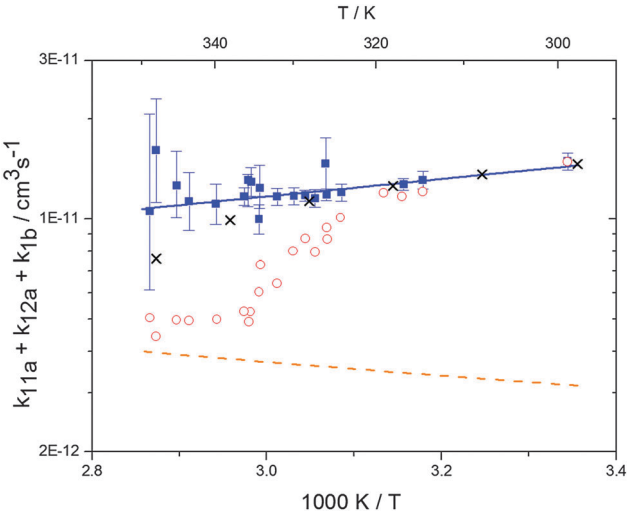

Fig. 2 Arrhenius plot of the total rate constant (k_{11a} + k_{12a} + k_{1b}) for the reaction OH + *p*-cymene. The blue solid line shows the Arrhenius curve for the total rate constants from the triexponential model (blue squares). Red open circles show the results of the biexponential model.[13] The orange dashed line shows the estimated H-atom abstraction for *p*-cymene.[13] Exes show simulated results from a combined theoretical/experimental approach (Section 6).

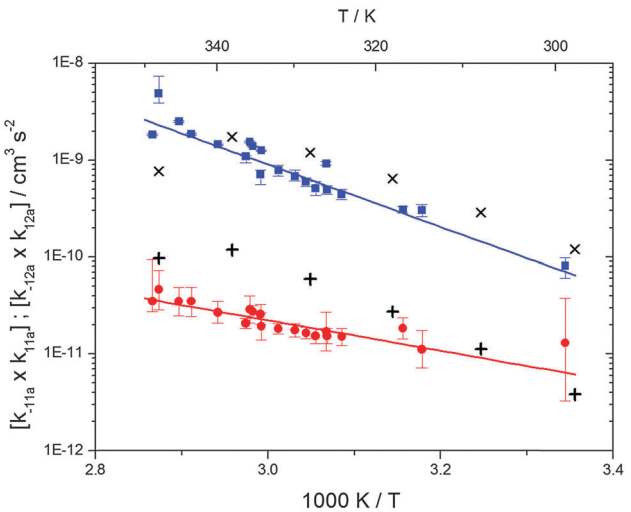

Fig. 3 Arrhenius plot for the product of the forward and backward reaction rate constants for the formation of adduct 1 (blue squares) and adduct 2 (red circles). Solid blue and red lines represent the Arrhenius curves for adduct 1 and 2, respectively. Exes and crosses show simulated results from a combined theoretical/experimental approach (Section 6) for adduct 1 and 2, respectively.

The product of the rate constants for the forward and backward reaction for both adducts increases with increasing temperature. Simple Arrhenius expressions of the form $k = A\exp(-B/T)$ were fitted to the data at temperatures between 299 and 349 K resulting in $k_{11a}k_{-11a} = 4\exp[(-7400 \pm 550)\ \mathrm{K}/T]\ \mathrm{cm}^3\ \mathrm{s}^{-2}$ for adduct 1 and $k_{12a}k_{-12a} = 1.2 \times 10^{-6}\exp[(-3620 \pm 1200)\ \mathrm{K}/T]\ \mathrm{cm}^3\ \mathrm{s}^{-2}$ for adduct 2. The sums of activation energies of forward and backward reactions were calculated from the *B* parameters to be (62 ± 5) kJ mol^{-1} and (30 ± 10) kJ mol^{-1} for adduct 1 and 2 respectively.

4.5 Unimolecular decay and background loss of the adducts (k_{-11a} + k_{31}; k_{-12a} + k_{32}) and adduct formation yields

Another combined rate constant that can be directly determined is the sum of the rate constants of unimolecular decay of the adducts back to the reactants and other products and of background losses by reactions with impurities. Possible perturbations by radical–radical reactions and diffusion processes have been already investigated.[5] While the unimolecular decay of the adducts strongly depends on the temperature, background reactions are assumed to be constant in the studied temperature range. Adduct loss rate constants for each adduct were fitted between 299 and 350 K to a function of the form $k = A\exp(-B/T) + C$. However, in a first step optimized parameters *C* (Fig. 4) were determined using expressions for the adduct yields and OH budget considerations.

Adduct formation yields were determined using eqn (12)–(15). The rate constants k_{1b} of H atom abstraction were taken from our previous work:[13] $k_{1b} = 2 \times 10^{-17}\ (T/\mathrm{K})^2\ \exp(170\ \mathrm{K}/T)\ \mathrm{cm}^3\ \mathrm{s}^{-1}$. At low temperatures, the denominators $(d - k_{31})$ and $(g - k_{32})$ are getting very small, making the obtained yields strongly dependent on k_{31} and k_{32}. Optimized values (7.5 ± 3.2) and (4.1 ± 0.3) s^{-1} were determined for k_{31} and k_{32}, respectively, that correspond to an average total yield of unity.

$$\Phi_1 = \frac{k_{11a}}{k_{OH}} = \frac{k_{11a}k_{-11a}}{k_{OH}k_{-11a}} = \frac{bc}{k_{OH}(d - k_{31})} \quad (12)$$

$$\Phi_2 = \frac{k_{12a}}{k_{OH}} = \frac{k_{12a}k_{-12a}}{k_{OH}k_{-12a}} = \frac{ef}{k_{OH}(g - k_{32})} \quad (13)$$

$$\Phi_{abst} = \frac{k_{1b}}{k_{OH}} \quad (14)$$

$$\sum \Phi_i = 1 \quad (15)$$

The various yields are shown in Fig. 5. The yields of adduct 1 and adduct 2 are similar at room temperature but then increase and decrease with temperature, respectively. Expectedly, the total adduct yield decreases with temperature because of an increasing yield of H-atom abstraction. Background loss rate constants were found to be in good agreement with those found in the literature for benzene,[20,21] toluene,[20,21] *p*-xylene,[22] 1,3,5-TMB[5] and hexamethylbenzene,[16] ranging from 2 to 8 s^{-1} Using the optimized values of k_{31} and k_{32}, Arrhenius expressions for the rate constants of unimolecular decompositions of the adducts were obtained: $k_{-11a} = 1 \times 10^{12}\exp[(-7600 \pm 800)\ \mathrm{K}/T]\ \mathrm{s}^{-1}$ and $k_{-12a} = 3 \times 10^{11}\exp[(-8000 \pm 300)\ \mathrm{K}/T]\ \mathrm{s}^{-1}$.

Activation energies for both adducts are very similar with values of 60 ± 7 and 67 ± 2 kJ mol^{-1} for adduct 1 and 2, respectively. These are rather similar to adducts formed from the OH radical addition to a non-occupied position as in the case of benzene (72 kJ mol^{-1}).[20] Fig. 4 shows the adduct loss rate constants for both *p*-cymene adducts in comparison with hexamethylbenzene[7] and both mesitylene[5] adducts. The dissociation rate constants found for the *p*-cymene adducts are very similar to the ones corresponding to the mesitylene

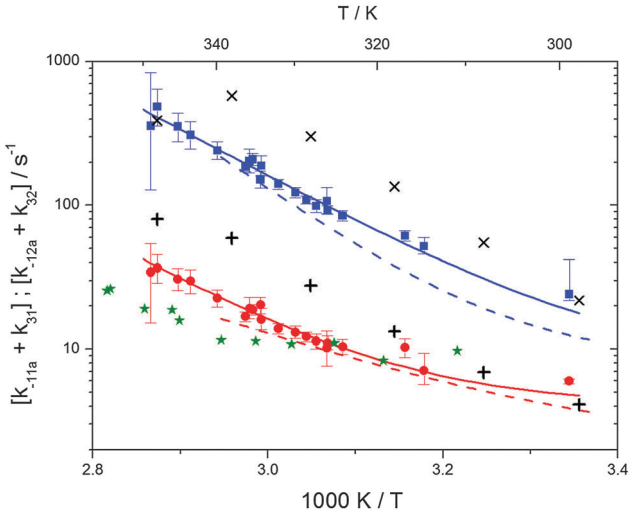

Fig. 4 Arrhenius plot for the sum of unimolecular and background loss rate constants for adduct 1 (blue squares) and adduct 2 (red circles), the hexamethylbenzene adduct (green asterisks).[7] The blue and red dashed lines show the rate constants of the *ortho* and *ipso* adduct of 1,3,5-trimethylbenzene.[5] Solid lines represent the modified Arrhenius curves for the adduct 1 and 2, respectively. Exes and crosses show simulated results from a combined theoretical/experimental approach (Section 6) for adduct 1 and 2, respectively.

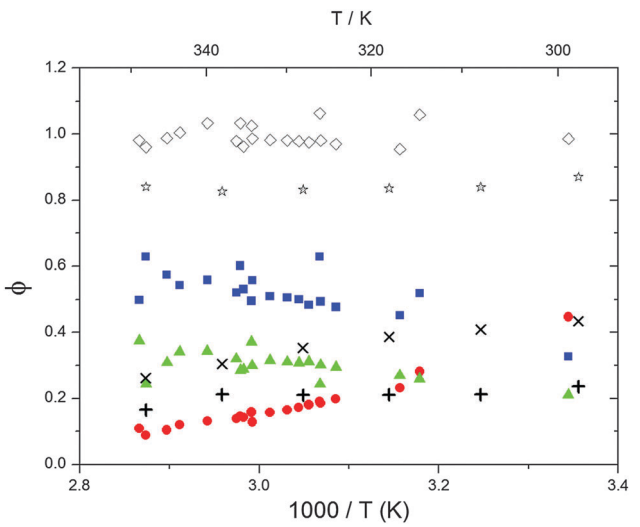

Fig. 5 Formation yields for adduct 1 (blue squares), adduct 2 (red circles) and H-atom abstraction (green triangles) after optimization of k_{31} and k_{32}. Rhombi show the sum of the calculated yields. Exes, crosses and asterisks show simulated results of a combined theoretical/experimental approach (Section 6) for adduct 1 and 2, and their sum, respectively.

adducts where only two isomers, *ipso* and *ortho*, can be formed. Furthermore, adducts 2 of *p*-cymene and mesitylene have low dissociation rate constants that are comparable to those obtained for hexamethylbenzene[16] where only *ipso* adducts are possible. The similarity of the activation energies of the adducts with the one of benzene, as well as the similarity of the dissociation rate constants of adduct 2 with the ones published for hexamethylbenzene make it very difficult to identify which adduct or group of adducts is responsible for the triexponential OH decays observed.

4.6 Equilibrium constants (K_{eq1}, K_{eq2}) and thermochemical data

A measure of the stability of the adducts is given by their equilibrium constants, K_{eq1}, K_{eq2} (Fig. 6). These constants were estimated using eqn (16) and (17) with background losses (k_{31} and k_{32}) determined in the previous section.

$$K_{eq1} = \frac{bc}{[d - k_{31}]^2} \quad (16)$$

$$K_{eq2} = \frac{ef}{[g - k_{32}]^2} \quad (17)$$

Equilibrium constants for both adducts are shown in Fig. 6 and can be expressed between 299 and 345 K by following equations:

$$K_{eq1} = 6.2 \times 10^{-26}\ (T/\mathrm{K})\ \exp[(7150 \pm 170)\ \mathrm{K}/T]\ \mathrm{cm}^3 \quad (18)$$

$$K_{eq2} = 2.3 \times 10^{-29}\ (T/\mathrm{K})\ \exp[(10\,200 \pm 1200)\ \mathrm{K}/T]\ \mathrm{cm}^3 \quad (19)$$

Standard reaction enthalpies and entropies were determined for each adduct using a van't Hoff expression (20). The values obtained were: $\Delta H_1 = (-59 \pm 1)$ kJ mol^{-1}, $\Delta S_1 = (-64 \pm 6)$ J mol^{-1} K^{-1} for the first and $\Delta H_2 = (-85 \pm 10)$ kJ mol^{-1}, $\Delta S_2 = (-130 \pm 27)$ J mol^{-1} K^{-1} for the second adduct.

$$K_{eq} = \frac{k_B T}{p^\theta} \exp\left(-\frac{\Delta H}{RT} + \frac{\Delta S}{R}\right) \quad (20)$$

The reaction enthalpy of adduct 2 is in reasonable agreement with results for other OH aromatics adducts from the literature.[23] However, the reaction enthalpy of adduct 1 is significantly smaller

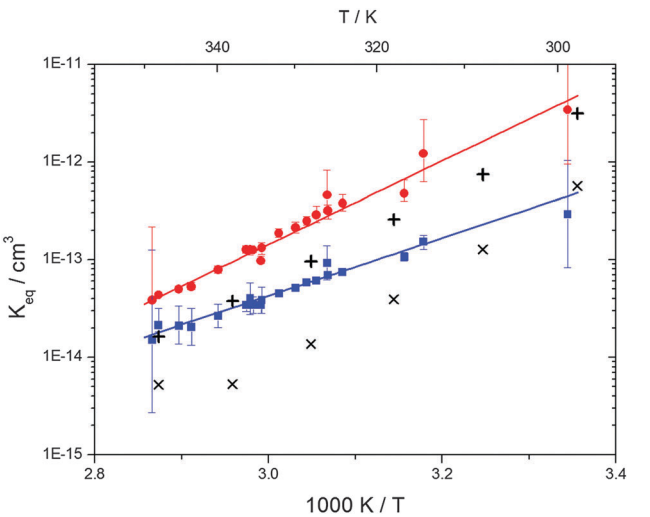

Fig. 6 Equilibrium constants for adduct 1 (blue squares) and adduct 2 (red circles). Solid lines represent the regression curves between 299 and 345 K (eqn (18) and (19)). Exes and crosses show the simulated results from a combined theoretical/experimental approach (Section 6) for adduct 1 and 2, respectively.

which is also in contradiction with theoretical predictions for different adduct isomers from other aromatics.[24–28] Moreover, the reaction entropy of adduct 1 is clearly too small for an association reaction and should in any case be very similar for both adducts. These inconsistencies point towards a perturbation possibly caused by the presence of more than two adduct species.

In our previous work,[13] the reduced χ^2 was applied to reject the simpler model for the formation of one single adduct. The mechanism proposed in the present work strongly improves the fit quality. However, despite the huge improvements reached by the triexponential model, there are still some high χ^2 values at temperatures between 330 and 340 K. These values might indicate the influence of further adduct species producing a departure from triexponential decays. To evaluate these deviations, OH decay curves with much higher precision would be needed as well as numerical tools to fit these curves but this is beyond our current capabilities.

5. Theoretical results

5.1 OH addition to *p*-cymene

As shown in Scheme 1, OH radical addition to the aromatic ring of *p*-cymene may form four isomers of *p*-cymene–OH adducts, two *ipso* isomers (PC_{ipso}–CH_3 and PC_{ipso}–C_3H_7) and two *ortho* isomers (PC_{ortho}–CH_3 or PC_{ortho}–C_3H_7). The correlation diagram between the relevant stationary states is illustrated in Fig. 7, and the corresponding zero-point corrected energies are gathered in Table 3. The pathways are initiated by the formation of the pre-reactive complex (PRC in Fig. 7) typical of electrophilic addition to aromatics[29] which corresponds to a long range interaction between *p*-cymene and the OH radical and is common to each addition channel. In this structure, the radical OH is situated above the aromatic ring. This PRC lies 26 kJ mol^{-1} below the energy of the separated reactants. On the way from the PRC to TS_{add}, the C–O distance diminishes from 2.5 Å to ~2.0 Å. It can be seen that the reactions are all exothermic by −85 kJ mol^{-1} in a narrow range of 5 kJ mol^{-1}. The $\Delta E_0^{\#}$ barriers, called TS_{add} in a generic way, are also very close together in a range between −2.4 and +2.5 kJ mol^{-1}. Such small values could suggest that the yields of *ipso* and *ortho* adducts are similar. In fact, the entropy change from the reactants to the TS is no more negligible and its value can be different from one pathway to the other. It is therefore essential to take into account the change of entropy in each pathway by calculating the Gibbs free energy barriers $\Delta G_T^{\#} = \Delta H_T^{\#} - T\Delta S_T^{\#}$ at temperature *T*. On the basis of the calculated $\Delta G_{298}^{\#}$ values, bimolecular OH-addition rate constants

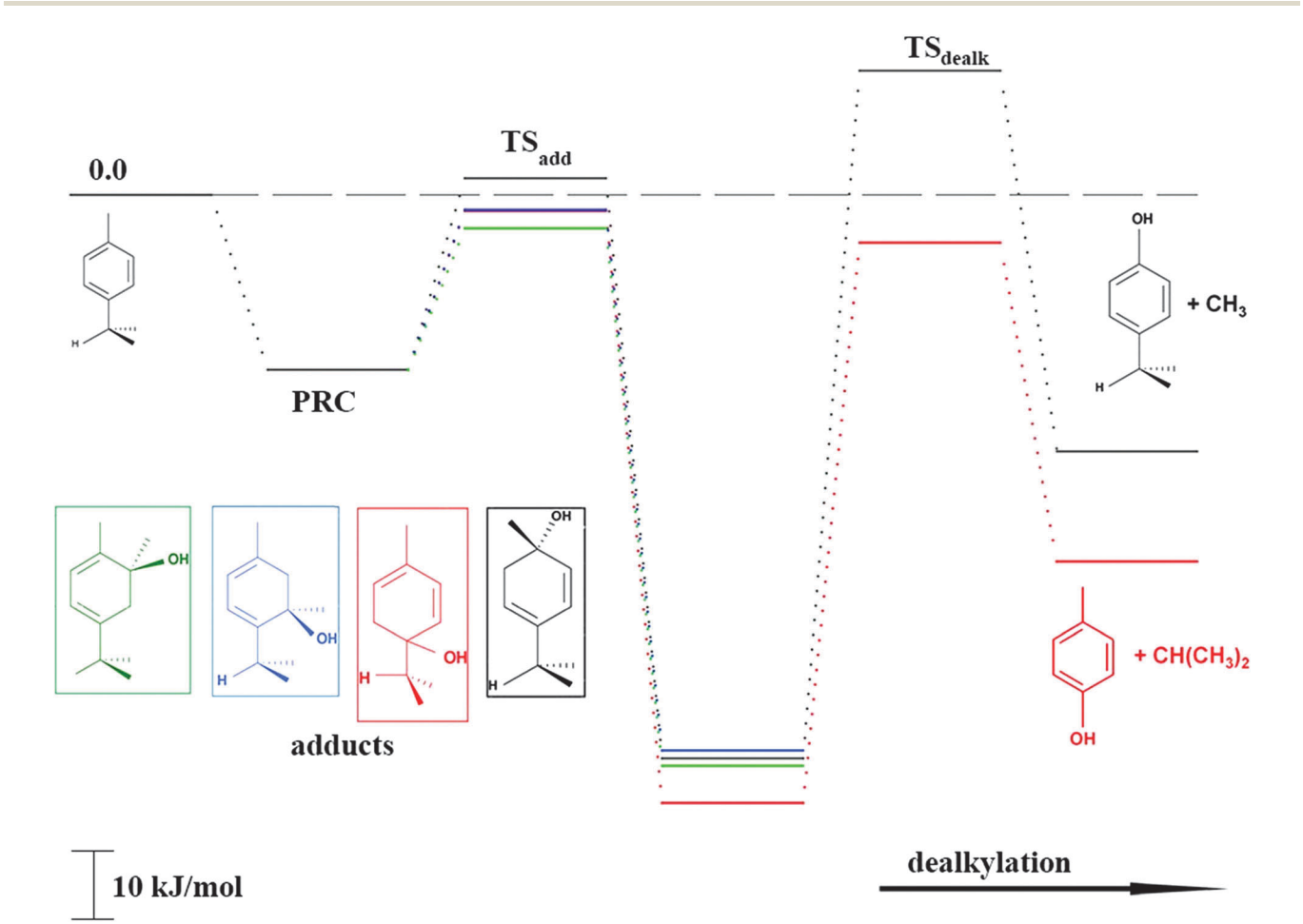

Fig. 7 Energy diagram for the addition reaction *p*-cymene + OH and successive dealkylation of the *ipso* adducts.

Table 3 M06-2X/6-31G(d,p) zero-point corrected energy barriers (ZPE), $\Delta E_0^{\#}$, activation enthalpies $\Delta H_{298}^{\#}$, activation entropies $\Delta S_{298}^{\#}$, free energy barriers, $\Delta G_{298}^{\#}$, and reaction energies, relative to the reactants *p*-cymene + OH,[a] and branching ratios, ρ_{add} (*i.e.* the percentage of each addition site). The ZPE barrier for dealkylation $\Delta E_0^{\#}$ (TS_{dealk}) and energy for cresol formation, ΔE_0 (cresol formation). The energy of the pre-reactive complex, ΔE_0 (PRC), is −25.9 kJ mol^{-1} [a,b]

	$\Delta E_0^{\#}$	$\Delta H_{298}^{\#}$	$\Delta S_{298}^{\#}$	$\Delta G_{298}^{\#}$	ΔE_0 adduct	ρ_{add} (%)	$\Delta E_0^{\#}$ TS_{dealk}	ΔE_0 cresol formation
PC_{ipso}–CH_3	2.5	−1.9	−149.8	42.7	−83.6	3	18.4	−38.1
PC_{ipso}–C_3H_7	−2.4	−6.6	−151.3	38.5	−90.3	18	−7.1	−52.3
PC_{ortho}–CH_3	−0.8	−5.1	−149.5	39.5	−84.7	24		
PC_{ortho}–C_3H_7	−2.2	−6.2	−146.3	37.4	−82.4	55		

[a] Energies are given in kJ mol^{-1}. [b] Entropies in J mol^{-1} K^{-1}.

were calculated from eqn (1). The branching ratios ρ_{add} are easily determined from the ratio of each rate constant channel over the total rate constant. All these data are collected in Table 3.

As a result of our calculations, it can be predicted that, among the four different addition possibilities: (i) the formation of the *ipso*-CH_3 adduct can be neglected from the reaction mechanism (3% of the total addition); (ii) the formation of *ortho* adducts is predominant (79%); (iii) the *ipso*-C_3H_7 adduct is formed (by 18% of total addition) but can further dissociate, *via* dealkylation, to give new products. This is the subject of the following section.

5.2 Formation of cresol by dealkylation of *ipso* adducts

PC_{ipso}–C_3H_7 and PC_{ipso}–CH_3 may dealkylate to form the phenol type compounds *p*-cresol + isopropyl radical (C_3H_7) and 4-isopropyl phenol + methyl radical (CH_3). The calculated transition state and reaction energies for both of these decompositions are sketched in the right part of Fig. 7. The overall reaction energies OH + *p*-cymene, leading to the formation of 4-isopropyl phenol + CH_3 or *p*-cresol + C_3H_7, are exothermic by −38 kJ mol^{-1} and −52 kJ mol^{-1}.

The corresponding free energies of activation, $\Delta G_{298}^{\#}$ for 298 K, suggest that only the isopropyl departure from the *ipso*-C_3H_7 adduct can occur at room temperature, since the energy barrier is lower by −7 kJ mol^{-1} than the energy of the reactants *p*-cymene + OH. In order to test this assumption, we have performed some preliminary kinetic calculations on this dealkylation channel by using a statistical approach based on a Rice–Ramsperger–Kassel–Marcus-like (RRKM)[30] methodology. Based on the potential energy profile obtained from DFT calculations, data presented in Table 3 was used for the kinetic analysis. For each of these stationary points, harmonic vibrational wavenumbers and the rotational constants calculated by the GAUSSIAN09 quantum chemistry program[18] were used. Table 4 summarizes these results at two temperatures and two pressures.

While there is no significant direct formation of cresol from OH + cymene, cresol is the main product of the unimolecular decomposition of the stabilized PC_{ipso}–C_3H_7 as indicated by the factor β. This finding is not in contradiction with product studies that showed no significant (<2%) cresol formation[11] because in the presence of O_2 cresol formation competes with the PC_{ipso}–C_3H_7 + O_2 reaction that is expected to be much faster under atmospheric conditions. However, in the absence of O_2, confirmation of cresol formation would be a strong indicator for the presence of the *ipso* adduct.

Table 4 Kinetic calculations on the dealkylation channel from the *ipso*-C_3H_7 adduct[a]

T/K	*P*/mbar	k_{loss}/ 10^{-13} cm^3 s^{-1}	k_{prod}/ 10^{-18} cm^3 s^{-1}	k_{adduct}/ 10^{-13} cm^3 s^{-1}	β
298	760	0.166	6.18	0.166	0.05
400	760	0.194	116	0.193	0.1
298	380	0.166	12.3	0.166	0.05

[a] k_{loss}: disappearance of the reactants for this addition channel; k_{prod}: immediate formation of products *p*-cresol + C_3H_7; k_{adduct}: stabilization of the *ipso* adduct; β: rate of regeneration of the reactants OH and *p*-cymene from the adduct divided by the formation of products *p*-cresol + C_3H_7 from the adduct.

5.3 Results for reaction entropies, enthalpies and equilibrium constants

Reaction entropies ΔS_{298}, reaction enthalpies ΔH_{298} and equilibrium constants K_{eq} have been calculated for the addition reactions at 298 K and are collected in Table 5, together with the corresponding experimental results obtained in this work. Calculated enthalpies are in good agreement with literature data for different OH adduct isomers from other aromatics.[23–28] As the *ipso*-CH_3 contribution is minor, and the *ipso*-C_3H_7 is expected to mainly dealkylate to cresol, the two adducts that are theoretically expected to determine OH regeneration are the remaining *ortho*-CH_3 and *ortho*-C_3H_7 adducts. Experimental entropy and enthalpy changes for adduct 1 are much smaller than those obtained from DFT calculations. This disagreement might arise from a wrongful application of the triexponential model to a system with three or four adducts, as mentioned in Section 4.6. Even though the obtained experimental enthalpy and entropy for adduct 2 are more comparable with the theoretical values, the experimental uncertainty does not allow to clearly identify this adduct. Nevertheless, the lower yields and greater equilibrium constants are closer to the predictions for the *ortho*-CH_3 adduct. In order to make the theoretical and experimental results more comparable, numerical simulations were performed and will be presented in the following section.

Table 5 Calculated M06-2X/6-31G(d,p) reaction entropies[a] ΔS_{298}, reaction enthalpies, ΔH_{298}, reaction free energies, ΔG_{298} at 298 K (relative to the reactants *p*-cymene + OH[b]) and calculated equilibrium constants, $K_{eq}(T) = k_B T/p^{\circ} \exp[-\Delta G_T/RT]$ for the four theoretically possible adducts and experimental results for comparison

	ΔS_{298} [a]	ΔH_{298} [b]	ΔG_{298} [b]	K_{eq} [c] (298 K)/10^{-13}
PC_{ipso}–CH_3	−161.1	−89.2	−41.2	7.0
PC_{ipso}–C_3H_7	−155.2	−95.3	−49.0	160
PC_{ortho}–CH_3	−154.0	−89.6	−43.7	19
PC_{ortho}–C_3H_7	−163.2	−87.9	−39.3	3.2
Adduct 1[d]	−64 ± 6	−59 ± 1	−40 ± 1	4.9
Adduct 2[d]	−130 ± 27	−85 ± 10	−46 ± 2	50

[a] Entropies in J mol^{-1} K^{-1}. [b] Energies in kJ mol^{-1}. [c] K_{eq} in cm^3. [d] This work (experimental).

6. Comparison of experimental and theoretical results using simulated OH decays

The theoretical results presented in the previous section predict the formation of all four possible adduct isomers. However, the relative yields and kinetic properties regarding back-decomposition and dealkylation are different for the different isomers. The question arises what results would be obtained from corresponding OH decay curves using the same data analysis that was applied for the experimental data of this work. To answer this question, OH decay curves were simulated by numerical calculations at a similar range of temperatures and reactant concentrations for direct comparison. For this purpose, a complete set of rate constants as a function of temperature is necessary.

We used the TST predicted adduct yields and the measured total rate constants of adduct formation (k_{add}) to make simulations and measurements more comparable. Values of k_{add} were obtained by subtracting the rate constants of abstraction k_{1b} from the k_{OH} obtained in this work:

$$k_{add} = k_{OH} - k_{1b} \quad (21)$$

using the Arrhenius expressions of k_{OH} and k_{1b} given in Sections 4.3 and 4.5. The total rate constant k_{OH} is considered to be a robust quantity that can be extracted from the experimental data without knowing the actual number of isomers formed. Using eqn (1) and the $\Delta H^{\#}_{298}$ and $\Delta S^{\#}_{298}$ data (Table 3), adduct yields ρ_T were calculated for six temperatures in a range 298–348 K and scaled with the corresponding k_{add}.

$$k_{add}(i) = k_{add} \times \rho(i) \quad (22)$$

Here i stands for the different isomers and the resulting individual rate constants $k_{add}(i)$ are listed in Table 6. It should be noted that the temperature dependencies of enthalpies and entropies are negligible (<1%) in the narrow range considered here. In a second step, the first-order rate constants of adduct dissociation back to OH + *p*-cymene, $k_{cym}(i)$ were determined from the equilibrium constants K_{eq} obtained from the theoretically calculated ΔH_{298} and ΔS_{298} of the adduct formation reactions (Table 5).

$$k_{cym}(i) = k_{add}(i)/K_{eq}(i) \quad (23)$$

For the PC_{ipso}–C_3H_7 isomer also the rate constants of cresol formation were calculated from the estimated ratios β of rate constants of back-dissociation and cresol formation for this isomer (Table 4).

$$k_{cresol}(PC_{ipso}\text{–}C_3H_7) = k_{cym}(PC_{ipso}\text{–}C_3H_7)/\beta \quad (24)$$

In Table 7 the obtained first-order rate constants $k_{cresol}(PC_{ipso}\text{–}C_3H_7)$ and the $k_{cym}(i)$ for all isomers are listed. The rate constants in Tables 6 and 7 reveal that theoretically only a slight variation of adduct yields with temperature is expected. Moreover, the yield of PC_{ipso}–CH_3 remains below 5% at all temperatures and the predicted main fate of PC_{ipso}–C_3H_7 is decomposition to cresol + C_3H_7.

Based on the rate constants in Tables 6 and 7, OH decay curves were simulated numerically using FACSIMILE (MCPA Software Ltd., Oxfordshire, UK) assuming a realistic OH starting concentration of 1×10^{10} cm^{-3}. Additional background loss rate constants of 3 s^{-1} for all adduct isomers and 10 s^{-1} for OH were also implemented to improve the comparability with experimental conditions. Decay curves were produced for five *p*-cymene concentrations in the range 0.8–4 $\times$ 10^{13} cm^{-3} as in the real experiments for the six temperatures under consideration. The obtained concentration profiles were then converted to count rates including background and finally to count numbers binned exactly as in the real experiments. Poisson random noise was added dependent on the count numbers and 150 single OH decay curves were accumulated to simulate the typical repetition of single shot experiments.

Table 6 k_{OH}, k_{1b} and individual rate constants of adduct formation $k_{add}(i)$ of four adduct isomers at different temperatures. The $k_{add}(i)$ were calculated from theoretically predicted isomer yields and the experimental total rate constant of adduct formation $k_{add} = k_{OH} - k_{1b}$

T/K	k_{OH}/ 10^{-11} cm^3 s^{-1}	k_{1b}/ 10^{-12} cm^3 s^{-1}	k_{add} (PC_{ipso}–CH_3)/ 10^{-12} cm^3 s^{-1}	k_{add} (PC_{ipso}–C_3H_7)/ 10^{-12} cm^3 s^{-1}	k_{add} (PC_{ortho}–CH_3)/ 10^{-12} cm^3 s^{-1}	k_{add} (PC_{ortho}–C_3H_7)/ 10^{-12} cm^3 s^{-1}
298.0	1.47	3.14	0.380 (3%)	2.06 (18%)	2.78 (24%)	6.35 (55%)
308.0	1.38	3.29	0.362	1.84	2.54	5.73
318.0	1.29	3.45	0.344	1.65	2.32	5.16
328.0	1.22	3.61	0.326	1.48	2.12	4.66
338.0	1.15	3.78	0.307	1.33	1.93	4.20
348.0	1.10	3.95	0.289 (4%)	1.19 (17%)	1.76 (25%)	3.78 (54%)

Table 7 First-order rate constants of cresol + C_3H_7 formation from the PC_{ipso}–C_3H_7 isomer and individual rate constants of OH + *p*-cymene formation $k_{cym}(i)$ from all four OH adduct isomers at different temperatures. The $k_{cym}(i)$ were calculated from theoretically predicted equilibrium constants and the $k_{add}(i)$ of Table 5. The ratios k_{cym}/k_{cresol} correspond to the theoretically predicted β (see Section 5.2)

T/K	k_{cresol} (PC_{ipso}–C_3H_7)/s^{-1}	k_{cym} (PC_{ipso}–CH_3)/s^{-1}	k_{cym} (PC_{ipso}–C_3H_7)/s^{-1}	k_{cym} (PC_{ortho}–CH_3)/s^{-1}	k_{cym} (PC_{ortho}–C_3H_7)/s^{-1}
298.0	2.56	0.545	0.128	1.48	19.8
308.0	7.06	1.62	0.387	4.24	54.6
318.0	18.1	4.46	1.08	11.3	141
328.0	43.8	11.5	2.83	28.0	339
338.0	99.5	27.6	6.93	65.6	769
348.0	214	62.7	16.0	145	1650

Table 8 Mean fit results and fit qualities with standard deviations from the analysis of numerically calculated OH decay curves and simulated experiments with random noise. Parameters correspond to those in Table 2 but standard deviations were obtained from 100 simulated experiments for each set of OH decay curves

T/K	k_2/s^{-1}	$k_{11a} + k_{12a} + k_{1b}$/ 10^{-11} cm^3 s^{-1} (=k_{OH})	$k_{11a}k_{-11a}$/ 10^{-10} cm^3 s^{-2}	$k_{12a}k_{-12a}$/ 10^{-11} cm^3 s^{-2}	$k_{-11a} + k_{31}$/s^{-1}	$k_{-12a} + k_{32}$/s^{-1}	χ^2/DOF
298.0	9.3 ± 1.1	1.464 ± 0.013	1.20 ± 0.02	0.38 ± 0.10	21.9 ± 0.6	4.1 ± 0.6	1.17 ± 0.10
308.0	8.9 ± 0.8	1.365 ± 0.014	2.91 ± 0.06	1.13 ± 0.07	55.1 ± 0.9	6.9 ± 0.3	1.12 ± 0.09
318.0	9.4 ± 0.7	1.258 ± 0.022	6.44 ± 0.28	2.73 ± 0.11	135.6 ± 3.3	13.3 ± 0.3	1.09 ± 0.09
328.0	10.1 ± 0.6	1.134 ± 0.034	12.0 ± 1.2	5.92 ± 0.21	303 ± 15	27.8 ± 0.6	1.07 ± 0.09
338.0	10.4 ± 0.8	0.996 ± 0.091	17.5 ± 7.1	11.8 ± 0.8	580 ± 110	59.0 ± 1.6	1.05 ± 0.08
348.0	11.2 ± 1.0	0.76 ± 0.11	7.7 ± 8.5	9.7 ± 8.5	390 ± 310	80 ± 38	1.04 ± 0.10

For each temperature simultaneous fits to the five decay curves at different *p*-cymene concentrations were then performed with the software tools developed for the experimental data. Fit results varied slightly when the procedure described in the last paragraph was repeated caused by the applied random noise. Experiment simulations and fits were therefore repeated 100 times to obtain mean values and standard deviations of fit parameters and fit qualities. The results are listed in Table 8 and shown as black symbols for direct comparison in Fig. 2–6.

Previous applications of the method showed that simulations based on the pure two-adduct model ((R1)–(R6)) exactly returned the rate constants used for the numerical calculations. Moreover, in these cases the mean fit quality parameter χ^2/DOF was unity.[5] This is the expected ideal result when experimental uncertainties are known as for the simulations. A significant deviation from unity therefore indicates a departure of the mechanism from the two-adduct model. In the case discussed here there is merely a slight deviation which is hardly significant. Thus within the simulated uncertainties OH decay curves are effectively triexponential in agreement with the two-adduct model. The explanation of course is that two of the four adduct isomers that are formed play a minor role because either their yield is low (PC_{ipso}–CH_3) or they mainly decompose to products other than OH (PC_{ipso}–C_3H_7).

While the OH background loss rate constant k_2 is reproduced in all cases, with increasing temperature the fitted k_{OH} tend to deviate from those applied in the simulations (Table 6). Note that this deviation is not accompanied by a decrease of fit quality, so there are compensating effects, and fit quality therefore is a necessary but not sufficient condition that a reaction model is correct. Moreover, in the presence of a fast decomposing adduct the range of useful temperatures for such an analysis is clearly limited as explained in Section 4.1. In the simulated measurements this limit is already reached around 340 K as is evident from the levelling off of adduct 1 rate constants at greater temperatures.

Expectedly, the parameters $k_{11a}k_{-11a}$ and $k_{12a}k_{-12a}$ roughly correspond to the products $k_{add}(PC_{ortho}\text{–}C_3H_7) \times k_{cym}(PC_{ortho}\text{–}C_3H_7)$ and $k_{add}(PC_{ortho}\text{–}CH_3) \times k_{cym}(PC_{ortho}\text{–}CH_3)$, respectively. And the parameters $k_{-11a} + k_{31}$ and $k_{-12a} + k_{32}$ more or less resemble $k_{cym}(PC_{ortho}\text{–}C_3H_7) + 3\ s^{-1}$ and $k_{cym}(PC_{ortho}\text{–}CH_3) + 3\ s^{-1}$, respectively, but the agreement is not perfect showing that the influence of the two *ipso*-isomers is not completely negligible even at the lowest temperature. Nevertheless, the further analysis reveals that the two adduct approach is also sufficient to extract reasonable values of adduct yields (Fig. 5) and equilibrium constants (Fig. 6) of the two adducts.

Moreover, the decomposition of the PC_{ipso}–C_3H_7 to cresol can be recognized by the fact that only about 90% of k_{OH} can be accounted for by $k_{11a} + k_{12a} + k_{1b}$. However, no such missing yield was recognized in the experiments that show no evidence for any unaccounted loss of OH.

Regarding the thermodynamic data, reaction enthalpies of −90 kJ mol^{-1} (adduct 1) and −89 kJ mol^{-1} (adduct 2) were obtained considering a temperature range <340 K that compare very well with the data applied to calculate the rate constants: −88 kJ mol^{-1} (PC_{ortho}–C_3H_7) and −90 kJ mol^{-1} (PC_{ortho}–CH_3). Reaction entropies are also in good agreement: −166 J mol^{-1} K^{-1} (adduct 1) and −146 J mol^{-1} K^{-1} (adduct 2) compared to −163 J mol^{-1} K^{-1} (PC_{ortho}–C_3H_7) and −154 J mol^{-1} K^{-1} (PC_{ortho}–CH_3) listed in Table 5. For all fit parameters in Fig. 2–6 a qualitative agreement is obtained but differences are clearly outside experimental uncertainties. Because the accuracies of the experimental and the theoretical approach are hard to quantify we conclude that the experimental results are not inconsistent with the theoretical prediction that the two experimentally distinguished adducts are PC_{ortho}–C_3H_7 (adduct 1) and PC_{ortho}–CH_3 (adduct 2).

7. Conclusions

The reaction *p*-cymene + OH was reinvestigated using a reaction model assuming formation of two adduct species. This model results in triexponential OH decay curves in the presence of *p*-cymene that can be evaluated to extract the rate constants of the underlying reaction model. Despite the fact that the reaction between *p*-cymene and OH radicals can form four different adducts (two *ipso*-type and two *ortho*-type adducts) observed OH decays fit to that model within experimental error. Good agreement with literature data was found for the rate constant of OH reaction at room temperature. In a temperature range been 299 and 349 K Arrhenius expressions for rate constants of the reaction model were obtained, as well as the yields of the supposed two adducts. Thermodynamic data were derived from temperature dependent equilibrium constants. For one adduct reasonable results were obtained but for the second adduct the reaction enthalpy and reaction entropy are not within expectations and probably influenced by the presence of further adduct species. DFT calculations were made that indeed predict the formation of all four possible adducts with different

yields. A full set of thermodynamic data for all relevant reactions was obtained. The formation of the two *ortho*-adducts was found to be predominant while the *ipso*-adducts are either almost negligible (*ipso*-CH_3) or react mostly by dealkylation rather than back-dissociation to OH and *p*-cymene (*ipso*-C_3H_7). This led to the conclusion that mainly the two *ortho* adducts were in equilibrium with OH and therefore detected in the experiments, resulting in triexponential OH decays. Finally, numerical simulations of OH decay curves were made using a combination of the theoretical results and measured OH rate constants. These decay curves were evaluated to quantify any departure from triexponential behavior and to reproduce the consequences of using the simplified reaction model. Results from these simulations show a qualitative agreement with experiments but differences are outside experimental uncertainties. The results from these simulations show a reasonable agreement with experimental results confirming the theoretical prediction that two distinguished adducts are PC_{ortho}–C_3H_7 (adduct 1) and PC_{ortho}–CH_3 (adduct 2).

Acknowledgements

This work was supported by the Deutsche Forschungsgemeinschaft under grant ZE 792/6-1 and BO 1580/3-1, and by CNRS/INSU within the French-German CNRS-INSU/DFG bilateral program ATMOCHEM. We thank Rafal Strekowski (University of Provence) for the first, exploratory experiments with *p*-cymene and OH and the group of Roger Atkinson (University of California, Riverside) for the determination of the abstraction and dealkylation channels.

References

1 S. D. Piccot, J. J. Watson and J. W. Jones, *J. Geophys. Res.: Atmos.*, 1992, **97**, 9897–9912.
2 A. Guenther, C. N. Hewitt, D. Erickson, R. Fall, C. Geron, T. Graedel, P. Harley, L. Klinger, M. Lerdau, W. A. McKay, T. Pierce, B. Scholes, R. Steinbrecher, R. Tallamraju, J. Taylor and P. Zimmerman, *J. Geophys. Res.*, 1995, **100**, 8873–8892.
3 R. Atkinson and J. Arey, *Atmos. Environ.*, 2003, **37**, 197–219.
4 J. G. Calvert, R. Atkinson, K.-H. Becker, R. M. Kamens, J. H. Seinfeld, T. J. Wallington and G. Yarwood, *The Mechanisms of Atmospheric Oxidation of Aromatic Hydrocarbons*, Oxford University Press, 2002.
5 B. Bohn and C. Zetzsch, *Phys. Chem. Chem. Phys.*, 2012, **14**, 13933–13948.
6 T. Berndt and O. Böge, *Int. J. Chem. Kinet.*, 2001, **33**, 124–129.
7 J. von Buttlar, R. Koch, M. Siese and C. Zetzsch, *Geophys. Res. Abstr.*, 2008, **10**, EGU2008-A-10576.
8 J.-C. Loison, M.-T. Rayez, J.-C. Rayez, A. Gratien, P. Morajkar, C. Fittschen and E. Villenave, *J. Phys. Chem. A*, 2012, **116**, 12189–12197.
9 J. Noda, R. Volkamer and M. J. Molina, *J. Phys. Chem. A*, 2009, **113**, 9658–9666.
10 D. F. Smith, C. D. McIver and T. E. Kleindienst, *J. Atmos. Chem.*, 1998, **30**, 209–228.
11 S. M. Aschmann, J. Arey and R. Atkinson, *Atmos. Environ.*, 2010, **44**, 3970–3975.
12 S. B. Corchnoy and R. Atkinson, *Environ. Sci. Technol.*, 1990, **24**, 1497–1502.
13 P. Alarcon, R. Strekowski and C. Zetzsch, *Phys. Chem. Chem. Phys.*, 2013, **15**, 20105–20114.
14 A. Wahner and C. Zetzsch, *J. Phys. Chem.*, 1983, **87**, 4945–4951.
15 R. Koch, R. Knispel, M. Elend, M. Siese and C. Zetzsch, *Atmos. Chem. Phys.*, 2007, **7**, 2057–2071.
16 S. Zhang, R. Strekowski, L. Bosland, A. Monod and C. Zetzsch, *Phys. Chem. Chem. Phys.*, 2011, **13**, 11671–11677.
17 S. Zhang, R. S. Strekowski, L. Bosland, A. Monod and C. Zetzsch, *Int. J. Chem. Kinet.*, 2011, **43**, 547–556.
18 M. J. Frisch, G. W. Trucks, H. B. Schlegel, G. E. Scuseria, M. A. Robb, J. R. Cheeseman, G. Scalmani, V. Barone, B. Mennucci, G. A. Petersson, H. Nakatsuji, M. Caricato, X. Li, H. P. Hratchian, A. F. Izmaylov, J. Bloino, G. Zheng, J. L. Sonnenberg, M. Hada, M. Ehara, K. Toyota, R. Fukuda, J. Hasegawa, M. Ishida, T. Nakajima, Y. Honda, O. Kitao, H. Nakai, T. Vreven, J. A. Montgomery Jr., J. E. Peralta, F. Ogliaro, M. Bearpark, J. J. Heyd, E. Brothers, K. N. Kudin, V. N. Staroverov, R. Kobayashi, J. Normand, K. Raghavachari, A. Rendell, J. C. Burant, S. S. Iyengar, J. Tomasi, M. Cossi, N. Rega, J. M. Millam, M. Klene, J. E. Knox, J. B. Cross, V. Bakken, C. Adamo, J. Jaramillo, R. Gomperts, R. E. Stratmann, O. Yazyev, A. J. Austin, R. Cammi, C. Pomelli, J. W. Ochterski, R. L. Martin, K. Morokuma, V. G. Zakrzewski, G. A. Voth, P. Salvador, J. J. Dannenberg, S. Dapprich, A. D. Daniels, Ö. Farkas, J. B. Foresman, J. V. Ortiz, J. Cioslowski and D. J. Fox, *Gaussian 09, Revision A.1*, Gaussian Inc., Wallingford, CT, 2009.
19 Y. Zhao and D. Truhlar, *Theor. Chem. Acc.*, 2008, **120**, 215–241.
20 R. Knispel, R. Koch, M. Siese and C. Zetzsch, *Ber. Bunsenges. Phys. Chem.*, 1990, **94**, 1375–1379.
21 R. Koch, *Kinetische Untersuchung der Folgereaktionen der OH-Addukte von aromaten mit NO, NO_2 und O_2 mit simultaner Auswertung von Kurvenscharen, PhD dissertation,* University of Hannover, 1992.
22 R. Knispel, *Reaktionen von OH-Radikalen mit Aromaten und Folgereaktionen entstandener OH-Addukte von Aromaten*, PhD dissertation, University of Hannover, 1993.
23 R. A. Perry, R. Atkinson and J. N. Pitts, *J. Phys. Chem.*, 1977, **81**, 296–304.
24 V. H. Uc, I. García-Cruz, A. Hernández-Laguna and A. Vivier-Bunge, *J. Phys. Chem. A*, 2000, **104**, 7847–7855.
25 I. Suh, D. Zhang, R. Zhang, L. T. Molina and M. J. Molina, *Chem. Phys. Lett.*, 2002, **364**, 454–462.
26 D. Johnson, S. Raoult, R. Lesclaux and L. N. Krasnoperov, *J. Photochem. Photobiol., A*, 2005, **176**, 98–106.
27 J. Fan and R. Zhang, *J. Phys. Chem. A*, 2006, **110**, 7728–7737.
28 J. M. Andino and A. Vivier-Bunge, in *Adv. Quantum. Chem.*, ed. E. G. Michael and S. J. Matthew, Academic Press, 2008, vol. 55, pp. 297–310.
29 I. V. Tokmakov and M. C. Lin, *J. Phys. Chem. A*, 2002, **106**, 11309–11326.
30 M. R. Berman and M. C. Lin, *J. Phys. Chem.*, 1983, **87**, 3933–3942.